

# LiNi<sub>0.5</sub>Mn<sub>1.5</sub>O<sub>4</sub> Porous Micro-cubes Synthesized by a Facile Oxalic Acid Co-precipitation Method as Cathode Materials for Lithium-Ion Batteries

Yushan Li<sup>1</sup>, Jin Wang<sup>1</sup>, Zhaofu Zhou<sup>1</sup>, Qingrong Yao<sup>1</sup>, Zhongmin Wang<sup>2</sup>, Huaiying Zhou<sup>2,\*</sup>, Jianqiu Deng<sup>1,2,\*</sup>

<sup>1</sup> School of Materials Science and Engineering, Guilin University of Electronic Technology, Guangxi, Guilin 541004, China

<sup>2</sup> Guangxi Key Laboratory of Information Materials, Guilin University of Electronic Technology, Guangxi, Guilin 541004, China

\*E-mail: [jqdeng@guet.edu.cn](mailto:jqdeng@guet.edu.cn) (Jianqiu Deng), [zhy@guet.edu.cn](mailto:zhy@guet.edu.cn) (Huaiying Zhou)

Received: 21 October 2018 / Accepted: 29 November 2018 / Published: 7 February 2019

---

Porous LiNi<sub>0.5</sub>Mn<sub>1.5</sub>O<sub>4</sub> (LNMO) micro-cubes have been synthesized via oxalic acid co-precipitation and sintering process. The sintering temperature has significant influence on the morphology and electrochemical performance of LNMO samples. The LNMO porous micro-cubes prepared by sintering at 770 °C are composed of the primary nanoparticles, and show the outstanding electrochemical properties. The discharge capacity of 116 mAh g<sup>-1</sup> can be obtained at 1 C-rate after 200 charge-discharge cycles. Even at 5 C, the porous micro-cubes exhibit a discharge capacity of 90.2 mAh g<sup>-1</sup>, corresponding to a capacity retention of 88.4% over 500 cycles. The excellent electrochemical performance may be ascribed to the porous cubic structure and the primary nanoparticles, which provide stable structure and short distance for lithium-ion diffusion.

---

**Keywords:** Lithium-ion batteries; Cathode; LiNi<sub>0.5</sub>Mn<sub>1.5</sub>O<sub>4</sub>; Porous micro-cubes; Co-precipitation method.

## 1. INTRODUCTION

The development of next-generation lithium-ion batteries (LIBs) is expected to play a key role in boosting the popularization of the electric vehicles (EVs) and hybrid-electric vehicles (HEVs). As a well-known cathode material for next-generation LIBs, spinel LiNi<sub>0.5</sub>Mn<sub>1.5</sub>O<sub>4</sub> (LNMO) with low cost and environmental friendliness offers a higher specific energy than that of LiCoO<sub>2</sub>, LiFeO<sub>4</sub>, and LiMn<sub>2</sub>O<sub>4</sub>, because of its high working voltage (4.7 V) and practical capacity (~130 mAh g<sup>-1</sup>) [1]. However, the excellent rate capacity and cycle performance of LNMO are influenced by many

unfavorable factors, including cationic ordering, the formation of a solid electrolyte interphase (SEI) layer, and the existence of  $\text{Li}_x\text{Ni}_{1-x}\text{O}$  impurity phase [2, 3].

To solve these issues, several strategies have been used to improve the electrochemical properties, such as surface modification [4], ion doping [5], creating nanostructures [6] and porous/hollow structures [7-9]. Porous/hollow structured materials are considered as an effective strategy to achieve remarkable rate capability and cycling stability [10]. The primary nanoparticles can provide short distances for Li-ion and electron diffusion and the larger surface area increases the reaction active sites. The internal pore space can effectively mitigate the volume change and structural strain of the active materials during cycling. LNMO with porous/hollow structure has been synthesized by impregnation method [11], sol-gel method [12], co-precipitation method [13] and hydrothermal method [14], etc. Among the various synthesis methods, the co-precipitation method is the most effective to prepare LNMO and meet the requirement of its large-scale industrial application on. It has been widely reported that porous/hollow LNMO was synthesized by co-precipitation method using  $\text{NH}_4\text{HCO}_3$  or  $\text{Na}_2\text{CO}_3$  as precipitators, delivering excellent rate capability and improved cycle performance [15-17].

Herein, we present that the LNMO with porous cubic structure synthesized by using a facile oxalic acid co-precipitation method. The formation process of porous cubic structure has been discussed in detail. The LNMO porous micro-cubes exhibit superior high-rate and cycle performances, with a first discharge capacity of about  $102 \text{ mAh g}^{-1}$  at 5 C and a capacity retention of 88.4% over 500 cycles.

## 2. EXPERIMENTAL SECTION

### 2.1 Synthesis of the LNMO porous micro-cubes

LNMO porous micro-cubes were synthesized by the oxalic acid co-precipitation method. First the raw materials  $\text{LiOH}\cdot\text{H}_2\text{O}$ ,  $\text{Ni}(\text{CH}_3\text{COO})_2\cdot 4\text{H}_2\text{O}$ ,  $\text{Mn}(\text{CH}_3\text{COO})_2\cdot 4\text{H}_2\text{O}$  (Li:Ni:Mn=2:1:3) and oxalic acid were dissolved in distilled water. The molar ratio of oxalic acid to transition metal ions was 3:2. Meanwhile, 15 wt% starch was added into the above solution. After stirring for 6 h at 80 °C, the obtained slurry was then dried under vacuum oven at 120 °C overnight. The products were obtained by sintering at 750, 770 and 800 °C for 12 h in the air atmosphere with a heating rate of  $3 \text{ }^\circ\text{C min}^{-1}$ , and accordingly denoted as LNMO-750, LNMO-770, and LNMO-800.

### 2.2 Physical characterizations

X-ray powder diffraction (XRD) patterns of the products were collected on a PIXcel<sup>3D</sup> X-ray diffractometer with Cu K $\alpha$  radiation of  $\lambda=1.5418 \text{ \AA}$  within the  $2\theta$  range  $10^\circ\text{--}90^\circ$  with a step size of  $0.02^\circ$ . The crystal structure was refined using the Rietveld method as implemented in the Fullprof software package. The morphologies and composition of the samples were investigated by using field emission scanning electron microscopy (FE-SEM, FEI QUANTA FEG 450). Transmission electron microscopy (TEM) and high resolution transmission electron microscopy (HRTEM) were carried out on a JEOL

2010F transmission electron microscope operated at 200 keV. Brunauer–Emmett–Teller (BET) specific surface area of the products was determined by the physical adsorption of N<sub>2</sub> on ASAP2020.

### 2.3 Electrochemical measurements

Electrochemical measurements were performed using CR2032-type coin cells. The cathodes were prepared by coating the slurry (80 wt% active materials, 10 wt% acetylene black and 10 wt% polyvinylidene difluoride (PVDF) binder were dispersed in N-methyl pyrrolidone (NMP) solvent) onto an aluminum foil and then dried in a vacuum oven at 110 °C overnight. The foil was pressed and punched into circular electrodes (1.4 cm in diameter). The loading weight of the active materials on the electrodes was about 6-7 mg cm<sup>-2</sup>. The coin cells were assembled in an argon-filled glove box. Pure lithium foil was used as the counter electrode. The electrolyte was a solution of 1 M LiPF<sub>6</sub> in ethylene carbonate (EC)/dimethyl carbonate (DEC) with a volume ratio of 1:1. The galvanostatic charge-discharge testing was conducted using a BT-2000 Arbin battery testing system in a range of 3.5–4.95 V (1C=148 mA g<sup>-1</sup>). Cyclic voltammetry (CV) and electrochemical impedance spectroscopy (EIS) were carried out on an electrochemical workstation (Solartron Modulab).

## 3. RESULTS AND DISCUSSION

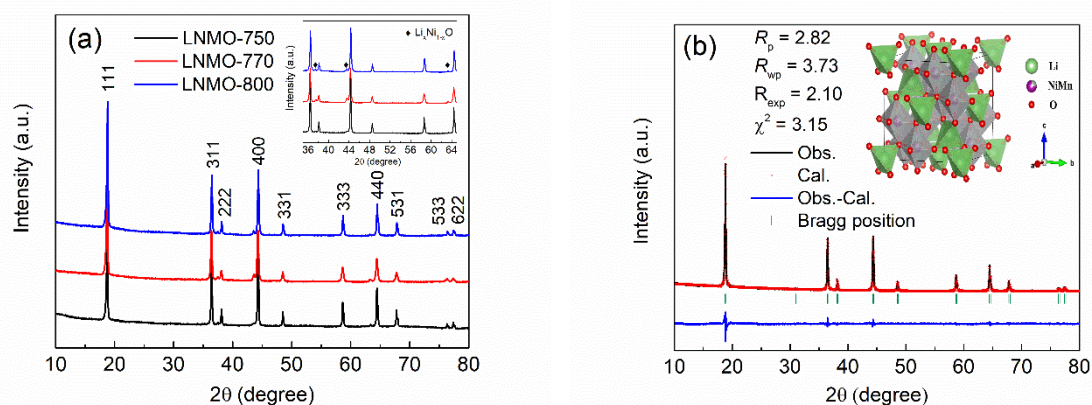


**Figure 1.** (a) XRD patterns of the as-prepared LNMO samples and (b) Rietveld refinement profiles of the XRD data for the LNMO-770 sample.

The XRD patterns of the as-prepared LNMO samples are shown in Figure 1. The diffraction peaks of the three samples are sharp indicating high crystallinity. The diffraction peaks can be well indexed into a cubic spinel structure (JCPDS No. 80-2162) with a space group of  $Fd\bar{3}m$  [18]. From Fig. 1, the very weak diffraction peaks at  $2\theta=37.7^\circ$  and  $43.7^\circ$  can be ascribed to the presence of rock salt impure phase ( $\text{Li}_x\text{Ni}_{1-x}\text{O}$ ), due to the loss of oxygen at high temperature [18, 19]. In order to obtain the lattice parameters of the samples, Rietveld refinement of XRD data was performed using the Fullprof software based on the spinel structure, as shown in Fig. 1b. The lattice parameters and cell volume of

the three samples are listed in Table 1. The negligible change of the lattice parameters in three samples indicates that the sintering temperatures from 750 to 800 °C hardly trigger any differences in their crystal structure. The obtained lattice parameters in this work are in accordance with the values for LNMO reported previously [20].

**Table 1.** Lattice parameters of LNMO samples prepared at three sintering temperatures.

Samples	a (Å)	b (Å)	c (Å)	V (Å <sup>3</sup> )
LNMO-750	8.1722	8.1722	8.1722	545.770
LNMO-770	8.1729	8.1729	8.1729	545.917
LNMO-800	8.1781	8.1781	8.1781	546.971

Figure 2 (a-c) presents the FE-SEM images of the LNMO-770 sample. The LNMO-770 sample shows complete and uniform-sized porous micro-cubic morphology. And the size of cubes is in a range of about 0.9–3.8 μm. From high-magnification FE-SEM image (Fig. 2c), the micro-cubes are composed of numerous primary nanoparticles with an average diameter about of 150 nm. The sintering temperatures have a large effect on the particle size and morphology of the prepared samples, as shown in Figure S1. When the sintering temperature remains 750 °C, the sample LNMO-750 is relatively compact and the pores on the surfaces of the micro-cubes is unclear. After the sintering temperature increases to 800 °C, the cubic morphology ruptures and transforms into irregular agglomerated particles consisted of nanosized subunits. The destruction of cubic morphology for LNMO prepared at 800 °C has been observed in previous work [21]. To further analyze the microstructure of the LNMO-770 sample, TEM and HRTEM were carried out. TEM image (Fig. 2d) confirms the porous structure of the LNMO-770 sample, which is in consistent with the SEM results. The HRTEM image (Fig. 2e) and selected area electron diffraction (SAED) pattern (Fig. S1f) further reveal the single crystal characteristics of primary nanoparticles, and the distance between adjacent lattice planes is about 0.472 nm, corresponding to the (111) planes of as-prepared spinel  $\text{LiNi}_{0.5}\text{Mn}_{1.5}\text{O}_4$ . The molar ratio Ni:Mn=1:2.95 of the LNMO-770 is determined by using energy dispersive spectrum analysis, being close to the designed compositions. BET measurements were performed to gain the surface area and the pore size distribution of the three LNMO samples, as shown in Fig. 2f. LNMO-770 has higher surface area (4.867 m<sup>2</sup> g<sup>-1</sup>) than that of both LNMO-750 (2.604 m<sup>2</sup> g<sup>-1</sup>) and LNMO-800 (2.328 m<sup>2</sup> g<sup>-1</sup>), which facilitates the contact between the electrode particles and the electrolyte, leading to better electrochemical performance.

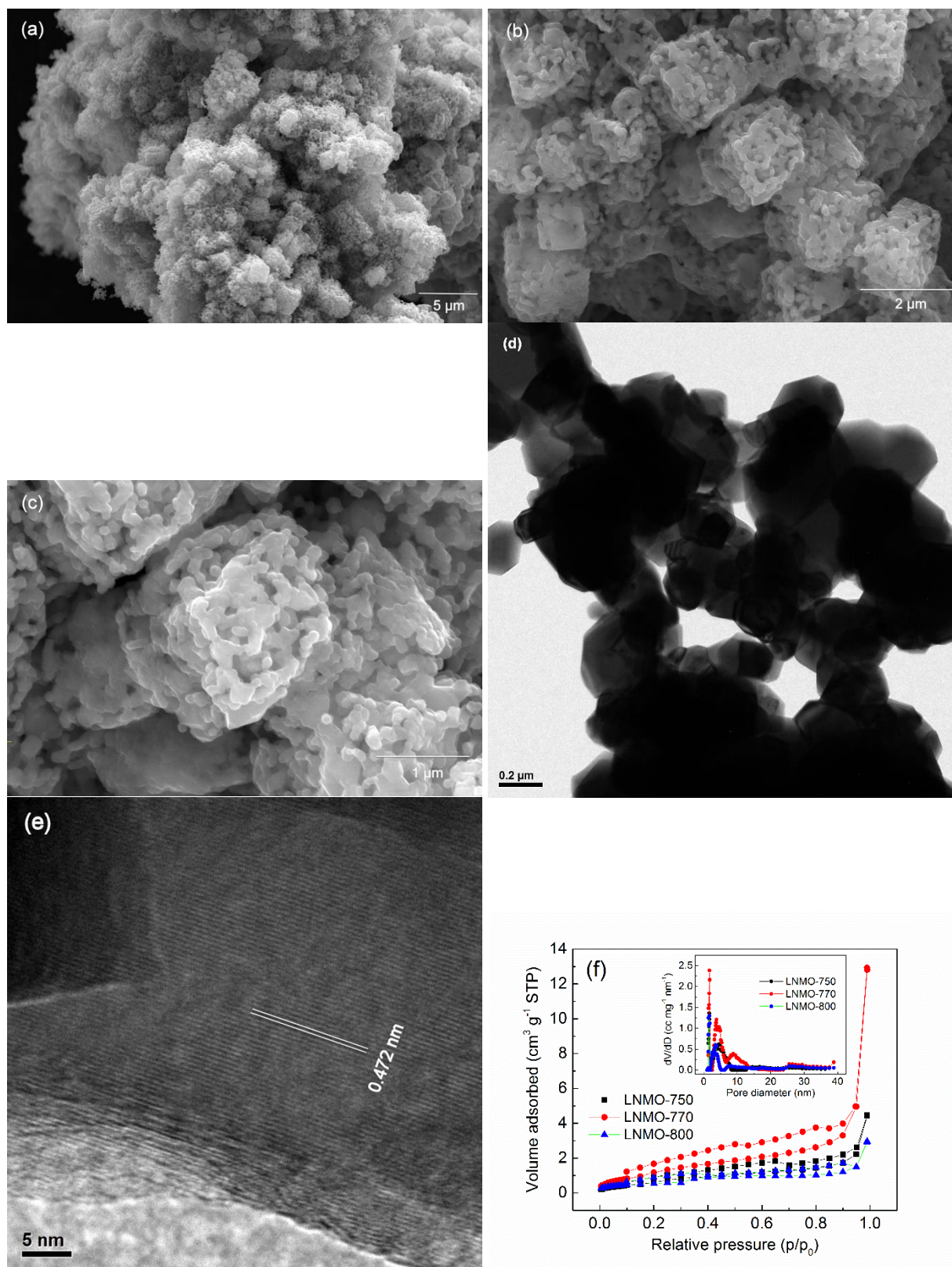


**Figure 2.** (a-c) SEM and (d, e) TEM images of the LNMO-770 sample, and (f) nitrogen isotherm adsorption/desorption curves of the LNMO samples.

Cyclic voltammetry (CV) was conducted to study the redox behavior of the LNMO samples between 3.5 and 4.95 V at a scan rate of  $0.1 \text{ mV s}^{-1}$ . Figure 3a shows the CV curves of three LNMO

samples. Two well-defined redox peaks between 4.6 and 4.8 V are observed, associated with  $\text{Ni}^{2+}/\text{Ni}^{4+}$  redox couples, respectively [5]. And a pair of minor redox peaks at around 4.0 V can be ascribed to the redox reaction of the  $\text{Mn}^{3+}/\text{Mn}^{4+}$  couple [13], indicating the existence of  $\text{Mn}^{3+}$  ions in the samples. The CV curves of the LNMO samples tested at various scan rates of 0.1, 0.2, 0.5 and 1.0  $\text{mV s}^{-1}$  are shown in Fig. 3b and Figure S2. With increasing scan rate, the peak current ( $i_p$ ) increases and potential separation within each redox couple widens. In addition, two obvious redox peaks can be observed in the CV curves, even for the highest scan rate of 1.0  $\text{mV s}^{-1}$ .

As illustrated in Fig. 3b, the highest oxidation peak current ( $i_p$ ) is proportional to the square root of scan rate ( $v^{1/2}$ ), indicating that electrode reaction is controlled by ion diffusion behavior. The diffusion coefficient of Li ions ( $D_{\text{Li}}$ ) can be calculated based on the Randles-Sevcik equation [22]

$$i_p = (2.69 \times 10^5) n^{3/2} A D_{\text{Li}}^{1/2} v^{1/2} C_{\text{Li}} \quad (1)$$

where  $i_p$  is the peak current (A),  $n$  is the number of electrons per reaction species,  $A$  is the surface area of the electrode ( $1.54 \text{ cm}^2$ ),  $D_{\text{Li}}$  is the diffusion coefficient of Li ions ( $\text{cm}^2 \text{ s}^{-1}$ ),  $v$  is the scan rate ( $\text{V s}^{-1}$ ), and  $C_{\text{Li}}$  is the bulk concentration of Li ions in the electrode ( $0.02378 \text{ mol cm}^{-3}$ ). The diffusion coefficients of three samples, as listed in Table S1, are in the order of  $10^{-11} \text{ cm}^2 \text{ s}^{-1}$ . And the sample LNMO-770 presents the highest value of the diffusion coefficient ( $2.8 \times 10^{-11} \text{ cm}^2 \text{ s}^{-1}$ ), which implies the fastest Li-ion intercalation kinetics, leading to its high-rate performance.

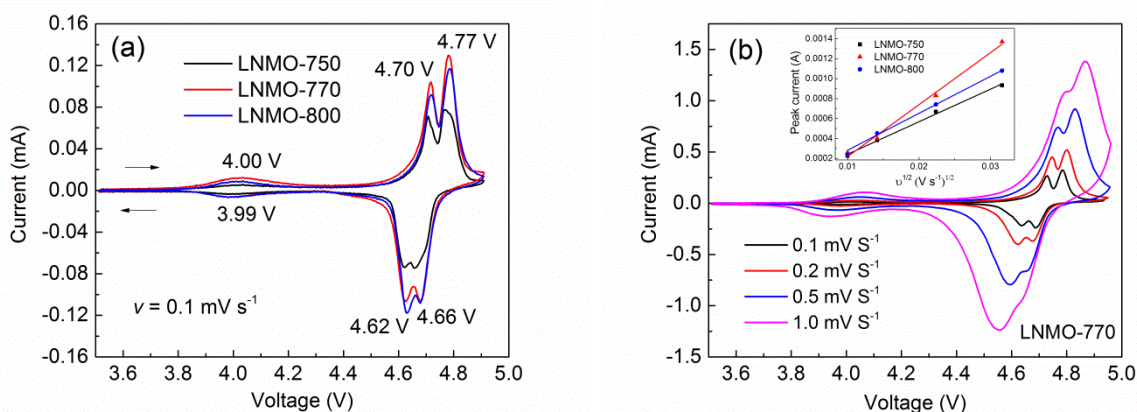


**Figure 3.** (a) CV curves of the LNMO three samples at a scan rate of 0.1  $\text{mV s}^{-1}$ , (b) CV curves the LNMO-770 sample at various scan rates, the inset is the plots of the highest oxidation peak currents and the square root of scan rates.

The electrochemical properties of the three samples were investigated by the galvanostatic charge–discharge testing. Figure 4a and Figure S3(a, b) shows the galvanostatic charge/discharge curves of the LNMO samples at a current density of 1 C ( $1\text{C}=148 \text{ mA g}^{-1}$ ) within a voltage range of 3.5–4.95 V. Two pairs of charge/discharge plateaus can be observed at about 4.6–4.7 V, associated with the  $\text{Ni}^{2+}/\text{Ni}^{4+}$  redox processes in LNMO. A small plateau at approximately 4.0 V is also clearly observed, corresponding to the redox reaction of the  $\text{Mn}^{3+}/\text{Mn}^{4+}$  couple. The charge/discharge plateaus in the charge–discharge curves are in agreement with the redox peaks observed in CV curves. The initial discharge capacities of the LNMO-750, LNMO-770 and LNMO-800 samples are 103.0, 108.0 and 96.5  $\text{mAh g}^{-1}$ , with a coulombic efficiency (CE) of 75.1%, 93.6%, and 76.8%, respectively. The coulombic

efficiency of the samples is close to 100% after 10 cycles. As presented in Fig. 4b, the LNMO-770 sample delivers the best cycle performance. The discharge capacity gradually increases to  $116.1 \text{ mAh g}^{-1}$  after 30 cycles, then can still keep a stable value over 200 cycles. Accordingly, the excellent rate capability is also observed in LNMO-770 sample, as shown in Fig. 4c. The discharge capacities are 103.4, 110.3, 113.2, 111.5, 108.0 and  $99.0 \text{ mAh g}^{-1}$  at 0.1, 0.2, 0.5, 1, 2 and 5 C, respectively. The capacity can recover to the initial value when the current density returns to 0.1 C, indicating superior cycle reversibility and structural stability of the samples. The excellent cycle and rate performance of LNMO-770 sample can be attributed to the synergistic effect of the porous cubic structure and primary nanoparticles. The pores and large surface area can facilitate to enhance the contact between LNMO and the electrolyte, leading to high capacities. The porous cubic structure can accommodate the volume change of LNMO during charge-discharge process, keeping the structural stability and improving cycle performance. In addition, the primary nanoparticles provide the short distance for lithium-ion diffusion, contributing to high capacities and superior rate capability.

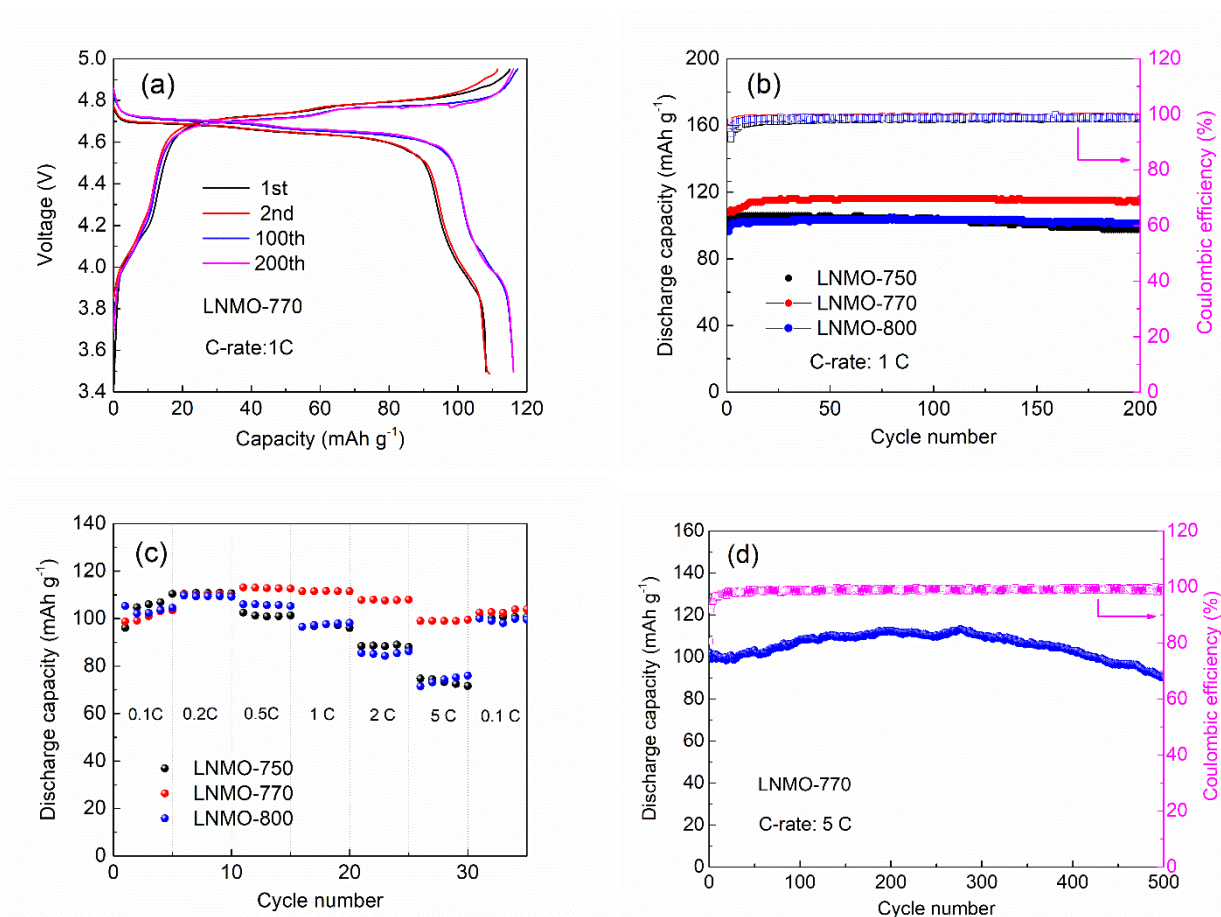


**Figure 4.** Electrochemical performance of the LNMO samples. (a) Galvanostatic charge–discharge curves of the LNMO-770 sample at 1 C, (b) cycle performance of the LNMO samples at 1 C, (c) rate capability of the LNMO samples, (d) long cycle life of the LNMO-770 samples at 5 C.

To further investigate the long cycle performance of the active materials, the LNMO-770 sample was tested by charging/discharging at 5 C rate. The corresponding results are displayed in Fig. 4d and Fig. S3d. The discharge capacity of the LNMO-770 sample is  $102.0 \text{ mAh g}^{-1}$  at the first cycle, and keeps

90.2 mAh g<sup>-1</sup> over 500 cycles at 5 C, with a capacity retention of 88.4%, indicating that the sample exhibits superior long-term cycle performance at a high current density. The long cycle performance of the LNMO-770 sample is comparable to previous reported porous LNMO cathodes (Table 2), confirming the superiority of the LNMO-770 sample in this work.

**Table 2.** A comparison of the cycle performance of LNMO-770 sample and previous reported porous LNMO materials.

Cathode materials	Cycle performance at 1 C	Cycle performance at 5 C	Ref.
Porous LNMO spheres	122 mAh g <sup>-1</sup> (1 <sup>st</sup> cycle), 115.4 mAh g <sup>-1</sup> (200 <sup>th</sup> cycle)	–	[11]
LNMO hollow microspheres	110 mAh g <sup>-1</sup> (1 <sup>st</sup> cycle), 95 mAh g <sup>-1</sup> (500 <sup>th</sup> cycle)	–	[16]
Porous LNMO microcubes	138.4 mAh g <sup>-1</sup> (1 <sup>st</sup> cycle)	–	[17]
LNMO micro-cubes	103 mAh g <sup>-1</sup> (50 <sup>th</sup> cycle) 119.6 mAh g <sup>-1</sup> (1 <sup>st</sup> cycle), 119 mAh g <sup>-1</sup> (100 <sup>th</sup> cycle)	116 mAh g <sup>-1</sup> (1 <sup>st</sup> cycle), 92.8% (300 cycles)	[21]
Hollow LNMO microspheres	ca. 122 mAh g <sup>-1</sup> (1 <sup>st</sup> cycle), 114.1 mAh g <sup>-1</sup> (500 <sup>th</sup> cycle)	ca. 114 mAh g <sup>-1</sup> (1 <sup>st</sup> cycle), 82.2% (500 cycles)	[23]
Cubic LNMO-770 sample	108 mAh g <sup>-1</sup> (1 <sup>st</sup> cycle), 116 mAh g <sup>-1</sup> (200 <sup>th</sup> cycle)	102 mAh g <sup>-1</sup> (1 <sup>st</sup> cycle), 88.4% (500 cycles)	This work

#### 4. CONCLUSIONS

The porous cubic LiNi<sub>0.5</sub>Mn<sub>1.5</sub>O<sub>4</sub> was successfully prepared by a simple oxalic acid co-precipitation method. The effects of sintering temperatures on the structure and electrochemical performance of LiNi<sub>0.5</sub>Mn<sub>1.5</sub>O<sub>4</sub> were investigated in details. The LiNi<sub>0.5</sub>Mn<sub>1.5</sub>O<sub>4</sub> sample prepared by sintering at 770 °C shows the porous micro-cube structure and the remarkable electrochemical performance. The porous LiNi<sub>0.5</sub>Mn<sub>1.5</sub>O<sub>4</sub> micro-cubes are composed of primary nanoparticles. The discharge capacity retains 116 mAh g<sup>-1</sup> after 200 cycles at 1 C. Even at 5 C, an initial discharge capacity is 102 mAh g<sup>-1</sup>, and the capacity retention keeps 88.4% after 500 cycles. The outstanding electrochemical performance is mainly ascribed to the uniform porous cubic structure composed of nano-sized subunits.

#### ACKNOWLEDGEMENTS

This work was funded by the National Natural Science Foundation of China (No. 51661009 and 51761007) and the Natural Science Foundation of Guangxi Province (2016GXNSFGA380001). This work was also jointly sponsored by Guangxi Key Laboratory of Information Materials (Guilin University of Electronic Technology), P.R. China (Project No. 171006-Z).

## SUPPORTING INFORMATION:

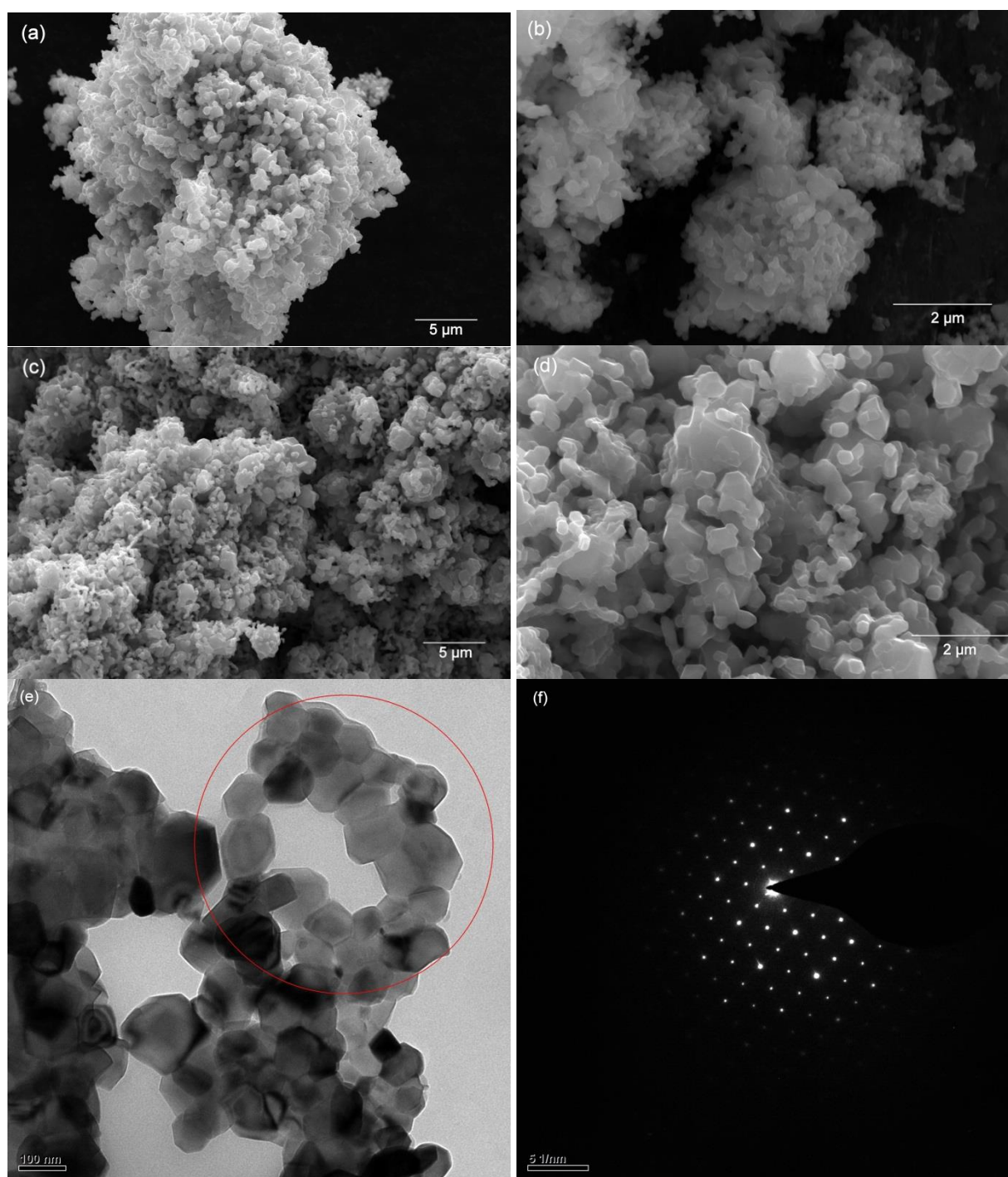


**Figure S1.** (a, b) SEM images of the LNMO-770 sample, (c, d) SEM images of the LNMO-800 sample, (e, f) TEM image and SEAD pattern for the LNMO-770 sample.

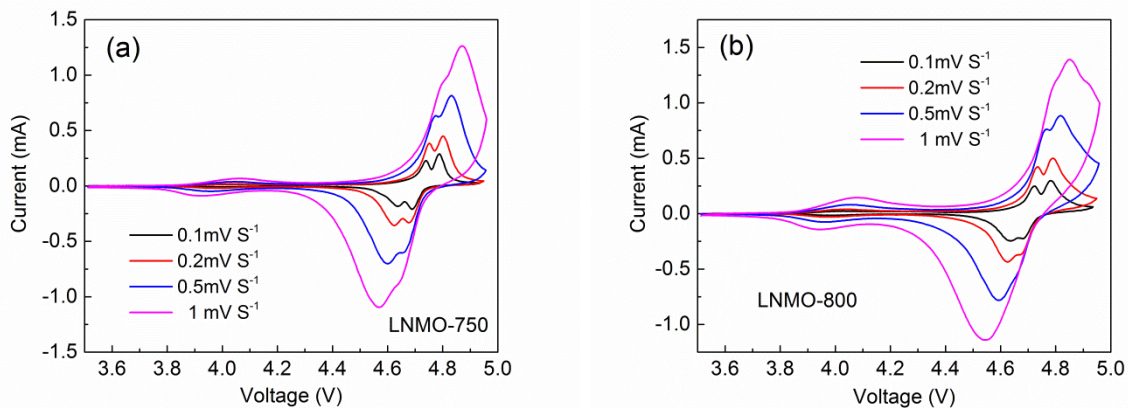


Figure S2. CV curves of the samples. (a) LNMO-750, (b) LNMO-800.

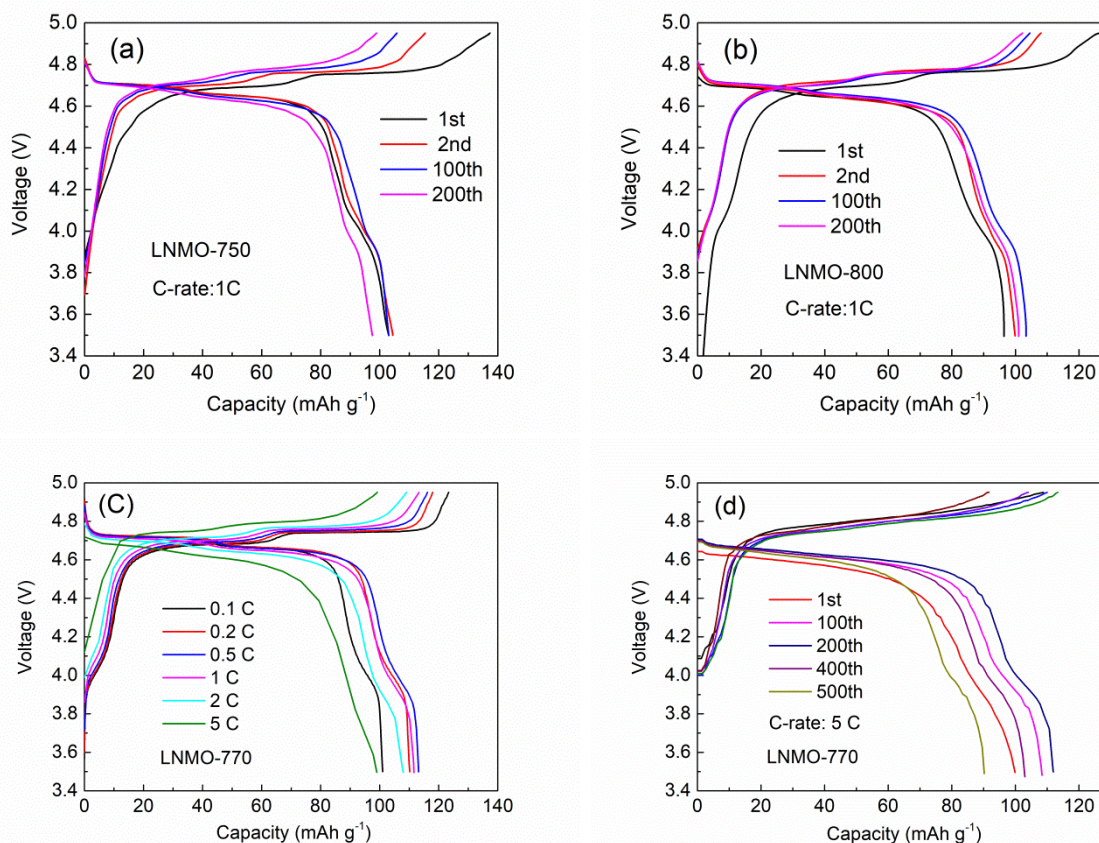


Figure S3. Charge/discharge curves of the three samples. (a) LNMO-750 sample at 1 C, (b) LNMO-800 sample at 1 C, (c) LNMO-770 sample at various C-rates, (d) LNMO-770 sample at 5 C.

Table S1. The diffusion coefficients of three samples obtained by CV technique.

Sample	LNMO-750	LNMO-770	LNMO-800
$D_{Li}$ (cm <sup>2</sup> s <sup>-1</sup> )	$1.09 \times 10^{-11}$	$2.8 \times 10^{-11}$	$1.41 \times 10^{-11}$

## References

1. T.-F. Yi, J. Mei and Y.-R. Zhu, *J. Power Sources*, 316 (2016) 85.
2. J. Ma, P. Hu, G. Cui and L. Chen, *Chem. Mater.*, 28 (2016) 3578.
3. M. Hu, X. Pang and Z. Zhou, *J. Power Sources*, 237 (2013) 229.
4. Y. Lin, Y. Yang, R. Yu, H. Lai and Z. Huang, *J. Power Sources*, 259 (2014) 188.
5. J. Wang, P. Nie, G. Xu, J. Jiang, Y. Wu, R. Fu, H. Dou and X. Zhang, *Adv. Funct. Mater.*, 28 (2018) 1704808.
6. X. Zhang, F. Cheng, J. Yang and J. Chen, *Nano Lett.*, 13 (2013) 2822.
7. J. Pan, J. Deng, Q. Yao, Y. Zou, Z. Wang, H. Zhou, L. Sun and G. Rao, *J. Power Sources*, 288 (2015) 353.
8. L. Wang, G. Liu, W. Wu, D. Chen and G. Liang, *J. Mater. Chem. A*, 3 (2015) 19497.
9. M. Lu, J. Wang, H. Fang, Y. Hu and J. Zhou, *Chem. Commun.*, 54 (2018) 4152.
10. K. Zhang, X. Han, Z. Hu, X. Zhang, Z. Tao and J. Chen, *Chem. Soc. Rev.*, 44 (2015) 699.
11. J. Wang, W. Lin, B. Wu and J. Zhao, *J. Mater. Chem. A*, 2 (2014) 16434.
12. H. Duncan, Y. Abu-Lebdeh and I.J. Davidson, *J. Electrochem. Soc.*, 157 (2010) A528.
13. Y. Yao, H. Liu, G. Li, H. Peng and K. Chen, *Mater. Chem. Phys.*, 143 (2014) 867.
14. X. Qin, J. Guo, M. Zhou, B. Zong, L. Wang and G. Liang, *Eur. J. Inorg. Chem.*, 2018 (2018) 1275.
15. Z. Zhu, D. Zhang, H. Yan, W. Li and Q. Lu, *J. Mater. Chem. A*, 1 (2013) 5492.
16. D. Lu, L. Yuan, Z. Chen, R. Zeng and Y. Cai, *J. Alloy. Compd.*, 730 (2018) 509.
17. S. Alagar, R. Madhuvilakku, R. Mariappan and S. Piraman, *J. Mater. Sci.-Mater. El.*, 29 (2018) 1173.
18. D. Liu, J. Hamel-Paquet, J. Trottier, F. Barry, V. Gariépy, P. Hovington, A. Guerfi, A. Mauger, C.M. Julien, J.B. Goodenough and K. Zaghib, *J. Power Sources*, 217 (2012) 400.
19. L. Wan, Y. Deng, C. Yang, H. Xu, X. Qin and G. Chen, *RSC Adv.*, 5 (2015) 25988.
20. C. Yin, H. Zhou, Z. Yang and J. Li, *ACS Appl. Mater. Inter.*, 10 (2018) 13625.
21. Y. Wu, J. Zhang, C. Cao, S. Khalid, Q. Zhao, R. Wang and F.K. Butt, *Electrochim. Acta*, 230 (2017) 293.
22. Z.-L. Zuo, J.-Q. Deng, J. Pan, W.-B. Luo, Q.-R. Yao, Z.-M. Wang, H.-Y. Zhou and H.-K. Liu, *J. Power Sources*, 357 (2017) 117.
23. Y. Xue, Z. - B. Wang, L.-L. Zheng, F. - D. Yu, B. - S. Liu and Y. - X. Zhou, *ChemistrySelect*, 2 (2017) 4325.